HOKKAIDO UNIVERSITY

Title	Evaluation of transport properties of deteriorated concrete due to calcium leaching with coupled CT image analysis and random walk simulation
Author(s)	Tan, Yingyao; Sugiyama, Takafumi; Hashimoto, Katsufumi
Citation	Construction and building materials, 369, 130526 https://doi.org/10.1016/j.conbuildmat.2023.130526
Issue Date	2023-03-10
Doc URL	https://hdl.handle.net/2115/93985
Rights	© <2023>. This manuscript version is made available under the CC-BY-NC-ND 4.0 license http://creativecommons.org/licenses/by-nc-nd/4.0/
Rights(URL)	https://creativecommons.org/licenses/by-nc-nd/4.0/
Type	journal article
File Information	Yingyao Tan_Final draft.pdf

Hokkaido University Collection of Scholarly and Academic Papers : HUSCAP

Evaluation of transport properties of deteriorated concrete due to calcium leaching with coupled CT image analysis and random walk simulation

*Yingyao Tan*1, Takafumi Sugiyama*2, and Katsufumi Hashimoto*2*

**1 Environmental Material Engineering Laboratory, Graduate School of Engineering, Hokkaido University, Sapporo Japan*

**2 Environmental Material Engineering Laboratory, Faculty of Engineering, Hokkaido University, Sapporo Japan*

Abstract: Concrete may deteriorate when chronically in contact with water due to the leaching of calcium ions. This study conducted a natural diffusion test for calcium ions with a minute cylindrical specimen of 3 mm in diameter and 6 mm in height to determine leaching at 20 and 80 ℃ in 33 days. One piece of limestone as aggregate was inserted inside each specimen to investigate the effect of the interfacial transition zone (ITZ). Changes in mass transfer in the leaching and non-leaching regions in bulk cement paste were evaluated using synchrotron X-ray computed tomography (CT) in a micrometer order. A deeper dissolution front of $Ca(OH)_2$ inside the specimen was observed for a higher temperature leaching test. Random walk simulation was performed to obtain diffusion parameters. Results showed that the calcium diffusion coefficient of non-deteriorated ITZ is about ten times as high as that of the non-leaching region. For the leaching region, the diffusion coefficient is about 50 times and 100 times as high as that of the non-leaching region at 20 ℃ and 80 ℃, respectively. In addition, the $Ca(OH)_2$ dissolution front appeared deeper inside the specimen in the direction where aggregate is close or exposed to the dissolution front because of ITZ.

Keywords: Calcium leaching, diffusion parameter, synchrotron X-ray CT, Microstructure, Interfacial transition zone (ITZ), Random walk.

1. Introduction

Concrete is extensively used in underground radioactive waste facilities due to its stable chemical properties to fulfill the requirement of structural stability. The alteration due to underground environment occurs in bulk cement paste and interfacial transition zone. It has been reported that calcium leaches out when cement-based materials come in contact with groundwater for an extended period [1][2][3]. Therefore, it is necessary to evaluate the performance of the bulk cement paste and ITZ during the reaction with water. Diffusive transport of solutes in cement-based materials is closely related to the microstructure of cement paste, especially the pore structure characteristics. The transport of solutes changes the pore structure characteristics of cement-based materials. In their study, Jacques et al. [4] described the mechanism of dissolution of calcium hydrates and calcium leaching. Extensive time is required for experimental investigations on the deterioration of concrete caused by calcium leaching due to contact with water. However, recently developed microstructural analysis techniques, such as the non-destructive integrated CT-XRD method [5][6], allow for the investigation of the alteration of cement-based materials in micro-meter order. This method significantly accelerated the research on calcium leaching mechanisms over a short period of experimental time.

Regarding experimental techniques, various approaches have been widely used to characterize the transport properties of cement paste. These include the scanning electron microscope (SEM), optical microscopy, and mercury intrusion porosimetry (MIP) [7]. However, only limited information can be

obtained from the resulting images using these methods, and 3D pore structures cannot be acquired. As a non-destructive and non-invasive imaging technique to detect the 3D geometry of the specimen, X-ray microcomputed tomography (CT) has been applied in recent cement-based materials research to obtain remarkably detailed information on pore structure[8][9][10][11][12][13]. Additionally, some innovative techniques have been proposed to characterize the transport properties from the extracted pore structure of CT images. For example, Zhang [14] applied the finite element method to simulate the diffusion process of tritiated water through the extracted pore structure and to quantify the corresponding ion diffusivity. Cecen [15] used the shortest path algorithm to obtain the tortuosity distribution of the internal structure of fuel cell materials. Promentilla [16] utilized the random walk simulation method in his study to quantify tortuosity in hardened cement paste with different ages.

Previous studies have provided methodologies for quantifying the transport properties of sound-hardened cement paste [17][18]. However, these studies lack quantification of transport properties for deteriorated or leaching regions and ITZ in concrete. The microstructure of ITZ can be obtained using high-resolution CT imaging. The effect of ITZ on macro mechanical characteristics has already been investigated in a previous study [19]. The lack of quantification of transport properties in ITZ is primarily due to irregular and extremely thin geometry, which makes extracting the ITZ region from CT images difficult. Previous research studies have largely relied on macroscopic migration experiments to estimate ITZ transport qualities [19][20][21] or on calculating relative parameters by applying an empirical formula based on the porosity difference between ITZ and bulk cement paste [22]. Therefore, to effectively predict calcium leaching in concrete over extended periods, it is significantly important to investigate the transport properties in ITZ and in both the sound and deteriorated regions of concrete.

Due to the time-consuming characteristics of Ca leaching, accelerated degradation methods have been used in previous studies. However, the leaching response differs between the accelerated leaching test and the non-accelerated tests [23][24]. Thus, in this study, a 33-day of non-accelerated leaching test with different temperatures (20 ℃ and 80 ℃) was conducted on a minute cylindrical specimen of 3mm in diameter and 6mm in height. The microstructure of deteriorated specimen was investigated using synchrotron microtomography at SPring-8 in Hyogo, Japan, at a resolution of 2.46 μm per voxel. The diffusion parameter of the leached and non-leached regions was evaluated using random walk simulation, and the leaching and non-leaching regions were verified using in-situ XRD. To obtain the diffusion parameter of ITZ directly from CT images, the microstructure adjacent to the aggregate surface was reconstructed, and the regular shape of ITZ was obtained.

2. Materials and Experiment

2.1 Specimen preparation and non-accelerated leaching test

Specimens for the non-accelerated leaching test were obtained from ordinary Portland cement (OPC) paste with a water-to-cement ratio of 0.5. By mass, the oxide composition of cement was 65.01% CaO, 21.41% SiO_2, 4.84% Al_2O_3, 3.20% Fe_2O_3, 1.08% MgO, and 2.02% SO_3. The fineness of OPC in terms of Blaine specific surface area was 3200 cm^2/g. The cement paste was mixed and placed into a plastic mold with a dimension of 3 mm in diameter and 6 mm in height. Then, one piece of limestone (as aggregate) was gently inserted into the fresh cement paste. Specimens were demolded after 24 h and cured by being wrapped in a wet towel at 20±2 ℃ for four weeks prior to the leaching test. Following curing, the specimens were subjected to a non-accelerated leaching test for 33 days.

Leaching experiments were performed at 20℃ and 80℃, and the corresponding specimen was labeled LCW-20 and LCW-80, respectively. In the leaching test, each specimen was placed in a plastic bottle. 1 cm^3

of purified water was filled in the bottle as solvent. After leaving the specimen in the bottle for a specified number of days, the solvent was removed. The same volume of fresh solvent was immediately poured back into the bottle, repeating the leaching process until 33 days. Within 33 days, solvent was change 9 times for LCW-20, while solvent was changed 11 times for LCW-80. Setting more measurements for LCW-80 is to adapt to higher leaching amount. Every time solvent is changed, removed solvent would be diluted 50 times and calcium ion concentration was measured using inductively coupled plasma atomic emission spectroscopy (ICP-AES) method.

2.2 CT imaging and in-situ XRD measurement

Micro tomographic images were acquired at a resolution of 2.46μm/voxel using an X-ray computed tomography (CT) system at SPring-8, Hyogo, Japan, one of the world's largest third-generation synchrotron radiation facilities. During imaging, the specimen was positioned in the direction of monochromatic X-ray and exposed, followed by the capture of an X-ray camera. Raw data for reconstructing CT images were derived from the linear attenuation coefficient (LAC). Raw images with different angles were obtained by rotating the specimen at 0.12° in each step until a 180° rotation was completed. The reconstructed CT images were obtained by inverse Radon transformation [25]. A schematic illustration of synchrotron microtomography is shown in Fig.1. The details of CT imaging in SPring-8 have been described in the paper of Uesugi et al [26].

In X-ray diffraction (XRD) measurement, the same X-ray source was used but with the use of a white X-ray. The slit system extracted only the signal from the Region of Interest (ROI), and the diffracted X-ray was captured by the solid-state detector. ROI selection can be set in the gauge because the coordinate system in the CT measurement corresponds to that in the XRD measurement. As a result, the angle between the incident path and exit path, which corresponds to twice the diffraction angle (2θ), is fixed at 10° during the measurement, and the relationship between X-ray energy and the intensity of diffracted X-ray can be obtained.

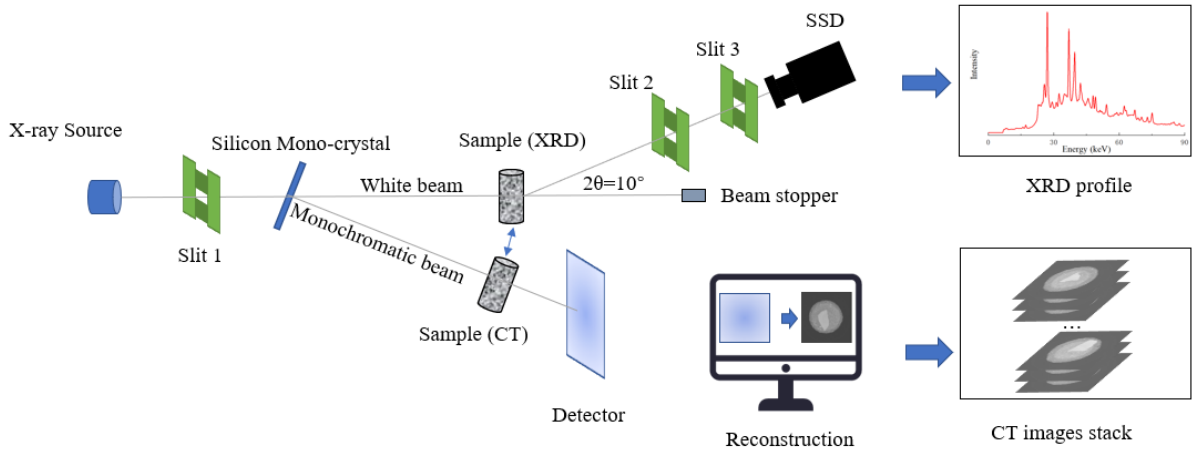


Fig.1 Schematic diagram of CT measurement and XRD measurement

The stack of CT slice images was used to obtain reconstructed 3-D volumetric data of the specimen. The reconstructed 3-D image data set was composed of 1440 contiguous slices, with each slice image containing 1440×1440 voxels. Normalization was applied to the whole stack of the reconstructed slices, as shown in Fig.2., to even out the brightness and contrast variation between slices and to enhance the contrast in the images. In CT measurement, the background around the specimen was also scanned, resulting in a

peak of around LAC=0 in the histogram of pixels' LAC value. The peak also covers some negative values, primarily as a result of the background noise.

In the normalization process, images were down-sampled from 32-bit to 8-bit grayscale images resulting in a smaller image file size. The volume of interest (VOI) was selected from the stack of CT slice images to avoid edge effects and reduce the computing time. Slice program [11] and ImageJ, a basic image analysis program, were used for the segmentation and cluster labeling of the normalized reconstructed grayscale images. The pore space was then extracted from VOI by thresholding them based on their gray-level histogram. Several approaches to pore segmentation have already been proposed in previous literature [27][28][29]. In this study, global thresholding was used to separate the pore from the 'solid' by defining the range of grayscale (GSV) associated with the pore voxel. The lower bound of GSV associated with pore voxels was set to 0, and the upper bound was set to the pore threshold value based on the transition point in the segmented porosity-threshold dependency curve, as detailed in the work of Promentilla et al [11].

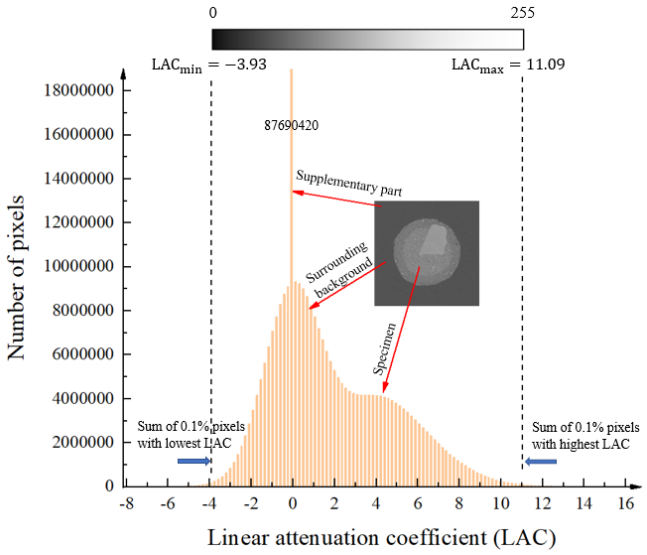


Fig.2 Schematic diagram of normalization

After pore segmentation, pore connectivity analysis was carried out using cluster labeling, commonly described in percolation theory [30]. In this analysis, two pore voxels were considered to be connected when they shared the same boundary surface. This cluster multiple labeling procedures enabled us to distinguish the largest percolating pore cluster from the other smaller isolated or dead-end pore clusters. Therefore, the largest percolating pore cluster is assumed to be the interconnected pores that most likely contribute to the macroscopic transport in the cement matrix.

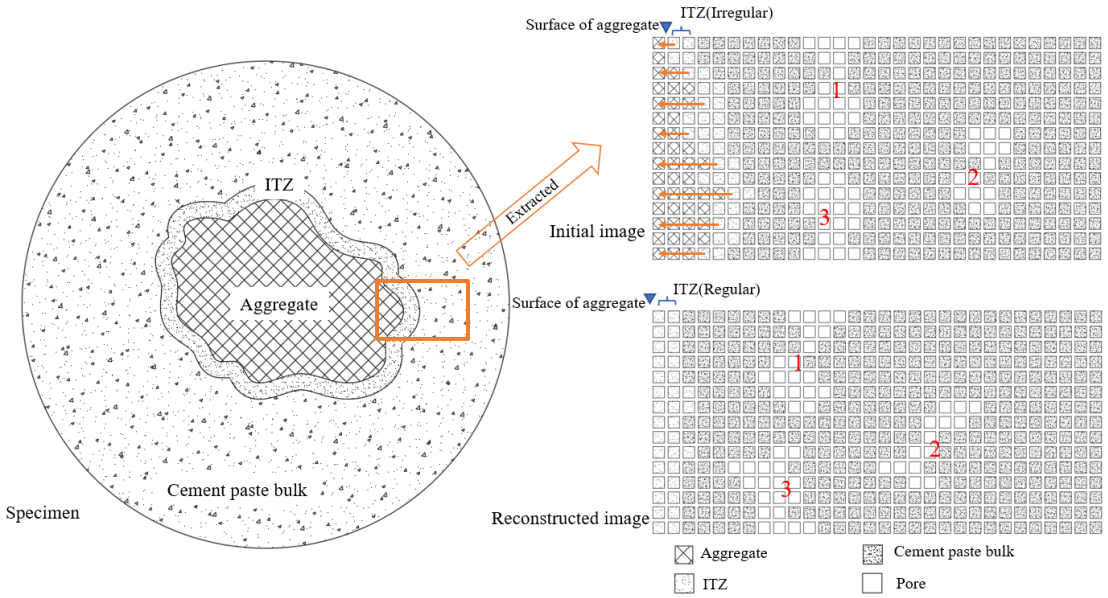


Fig.3 Schematic of reconstruction in one single slices

The interfacial transition zone (ITZ) around the aggregate is typically uneven in shape, making the extraction challenging. This study proposes an image reconstruction method for the regularly shaped ITZ region. Fig.3 depicts the schematic of reconstruction in a single slice. Pixels adjacent to the aggregate surface will be aligned on the same line, and irregularly shaped ITZ will become regular simultaneously. As shown in Fig.3, there are three labeled pores in the image before and after reconstruction, numbered 1, 2, and 3. Pore 1 becomes disconnected after reconstruction, while pore 2 becomes connected. The connectivity of pore 3 is unchanged, but its shape is altered. Reconstruction seemed to affect the topology of the pore, but when the direction away from the aggregate surface was used as the coordinate, the influence of reconstruction on different areas was the same. At the same time, considering the continuity of the aggregate surface, reconstruction would largely retain the original pore structure's characteristics.

3. Effective diffusion coefficient with Random walk simulation

Random walk simulation was performed on the largest percolating pore cluster to probe the pore geometry, quantify the diffusion tortuosity, and calculate the diffusion parameters. The 3D random walk technique in porous rocks was proposed [31] and applied to cement-based materials to investigate the transport properties [31][32][33]. It is based on the concept that the time-dependent diffusion coefficient $D(t)$ associated with the random Brownian motion of molecules can be utilized to probe the geometry of porous media. In a bulk medium, the self-diffusion coefficient of molecules is independent of time, but it is reduced and time-dependent in a confined geometry [34]. The self-diffusion coefficient approaches zero in closed pore space with a long diffusion time. However, the long-term behavior of the diffusion coefficient in the largest percolating pore cluster may approach a limiting value that can be used as a basis for probing connectivity and tortuosity.

The main output of a random walk simulation is the mean-square displacement (MSD, $\langle r^2 \rangle$) of the walkers as a function of lattice time t (Eq. (1)). The lattice time is incremented by a unit time after a random jump of the walker from one voxel to another. If the randomly selected voxel was a solid voxel, the jump was not performed, but the time still becomes $t+1$.

$$\langle r(t)^2 \rangle = \frac{1}{n}\sum_{i=1}^{n}\left[\left(x_i(t) - x_i(0)\right)^2 + \left(y_i(t) - y_i(0)\right)^2 + \left(z_i(t) - z_i(0)\right)^2\right] \quad (1)$$

Where n is the number of random walkers and $x_i(t)$, $y_i(t)$, and $z_i(t)$ are the 3-D coordinates of the walker's position at the time t for the ith walker.

Diffusion tortuosity (τ_D) is defined as the ratio of the self-diffusion coefficient D_0 of non-absorbing walkers in free space to the long-time self-diffusion coefficient D_∞ of these walkers in pore space [11][31][35], which also can be calculated as the ratio of MSD in free space to MSD in pore space (Eq. (2)).

$$\tau_D = \frac{D_0}{D_\infty} = \frac{\langle r(\tau)^2 \rangle_{free}}{\langle r(\tau)^2 \rangle_{pore}} \quad (2)$$

Tortuosity depends on how well the pores are connected in the porous medium. Macroscopically, tortuosity connects effective diffusion coefficient (D_e) and diffusion coefficient (D_f) in diluted solutions as well, as shown in Eq. (3) [36][37].

$$D_e = \frac{D_f}{F} = \frac{D_f \rho_e \delta}{\tau_D} \quad (3)$$

In Eq. (3), F is the electrical formation factor, the ratio of electrical conductivity of electrolyte in the bulk fluid to that in the porous medium [37]. By Nernst-Einstein relation, F connects diffusion coefficient in bulk fluid (D_f) and in porous medium (D_e), as ($F = D_f/D_e$). Specifically, D_f is the diffusion coefficient of Ca ion in water, here refers from ref[38]. ρ_e and τ_D are effective porosity and computed tortuosity respectively. ρ_e can be defined as ratio of voxels number of largest percolating pore cluster to the voxels number of the whole VOI while τ_D can be obtained through random walk simulation, which will be discuss in detail in the next section. δ is constrictivity, which is depended on the ratio of the diameter of the diffusing particle to the pore diameter. The diameter of calcium ion is much smaller than the smallest pore diameter (in this study, the smallest pore diameter equals the resolution of a CT image, 2.46μm × 2.46μm × 2.46μm). Then, it is assumed equal to 1 in this study.

4. Result and discussions

The amount of calcium ions dissolved from the specimen over time can be obtained by measuring the calcium ion concentration in the replaced solvent. Fig.4 shows the accumulated amount of calcium leaching per unit volume for each specimen over time. It is evident that higher temperature would result in higher leaching amount of Ca over the same leaching period and higher volume change, which would lead to a change in the pore structure.

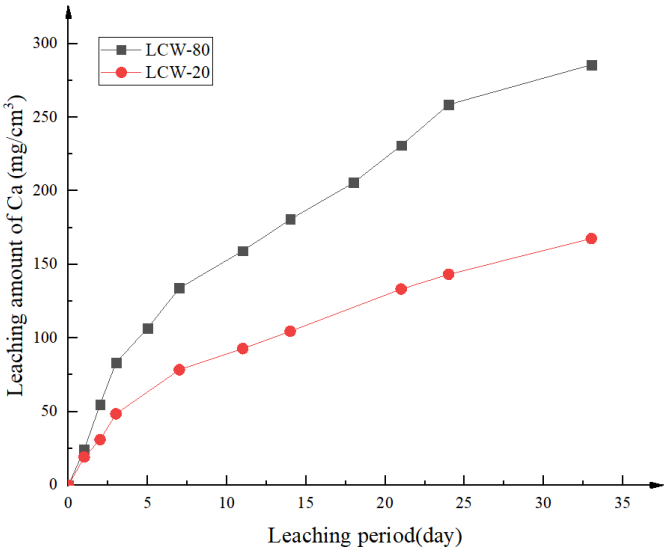


Fig.4 Leaching amount of Ca per unit volume of specimen

A 3-D image of each specimen consists of 1440 slices, to which 100 slices were extracted as representative samples for analysis, as shown in Fig.5. For LCW-20, slices from 650 to 749 were extracted, while for LCW-80, slices from 601 to 700 were extracted. The extraction principle is based on whether it could reflect the positional relationship between the aggregate and bulk cement paste.

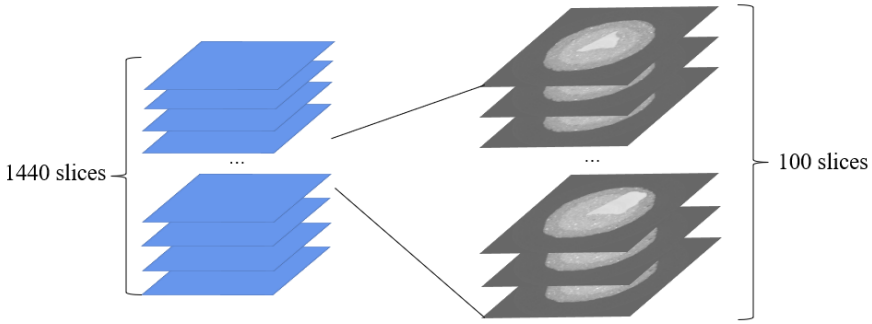
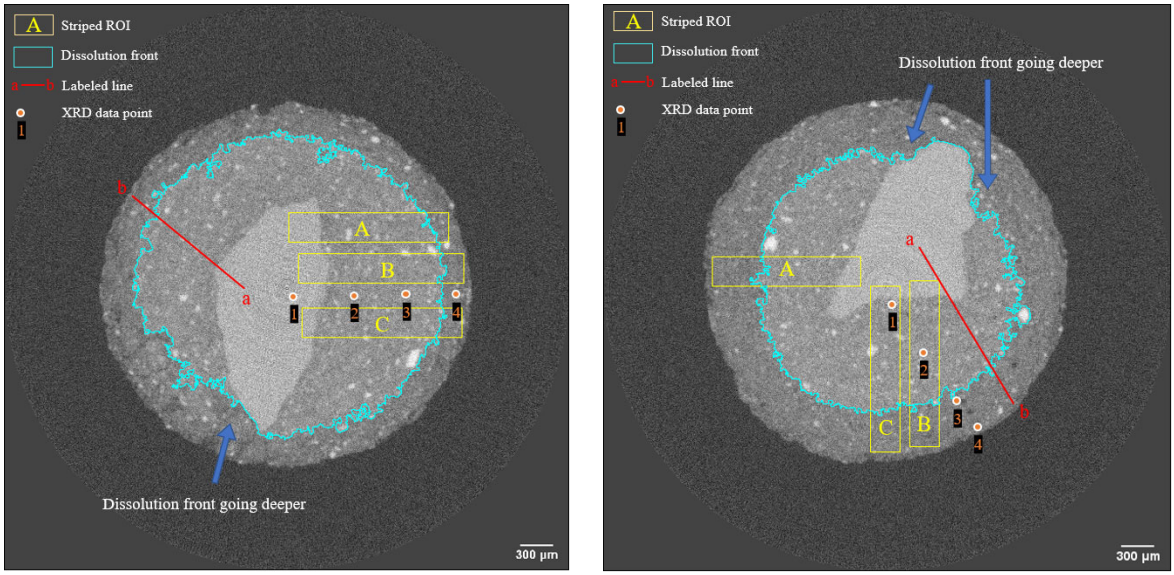


Fig.5 Stack of CT images

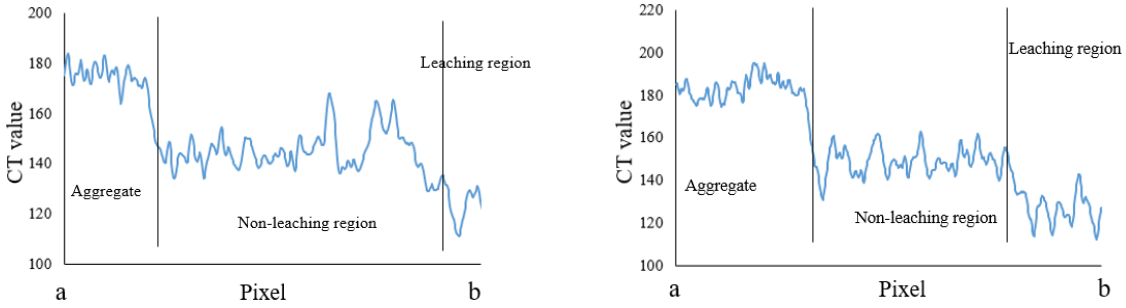
4.1 Leaching region and non-leaching region

Fig.6 (a) and (b) show the micro-tomographic images of each specimen with the following markings: striped ROIs, dissolution front, labeled line, and XRD data points. Three distinct gray scale regions can be observed inside the sample, which can be seen along the line marked a-b in Fig.7 (a) and (b). Aggregate generally contains minerals with higher LAC than hardened cement paste. However, LAC in degraded regions decreases due to the dissolution of portlandite or decalcification of C-S-H during leaching tests. Portlandite is one of the main components of cement hydration products and a relatively soluble part of hardened cement paste. Thus, regions with different grayscales can be defined as aggregate, non-leaching, and leaching regions, as shown in Fig.7(a) and Fig.7(b).



(a) LCW-20 (b) LCW-80

Fig.6 CT image of each specimen



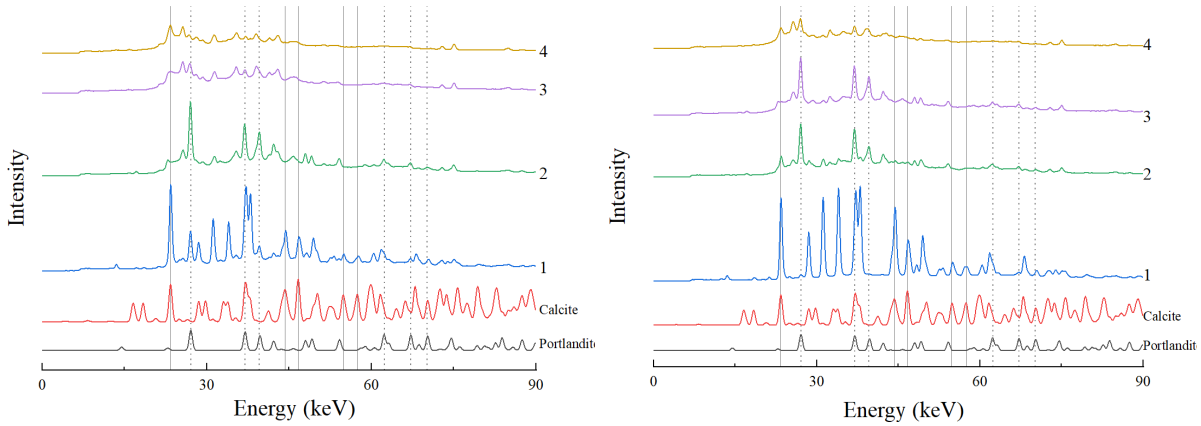
(a) LCW-20 (b) LCW-80

Fig.7 Gray scales changes along line a-b of each specimen

In-situ XRD analysis was applied to points within each specimen, the locations of which are shown in Fig.6. The result of XRD analysis for each point of interest is shown in Fig.8. In this figure, the peaks that coincide with the characteristic peak of portlandite were marked accordingly. It can be observed that the marked peaks of portlandite are visible in both the non-leaching and leaching regions. However, the intensity of the marked peaks is higher for points located in the non-leaching region. In the non-leaching region, the intensity of marked peaks of portlandite does not show a significant difference, while for points in the leaching region, the intensity of portlandite peaks decreases along the direction close to the specimen edge. This implies that portlandite has dissolved in the leaching region. The interface, denoted by the blue line in Fig.6, between the leaching and non-leaching regions can be considered the dissolution front of portlandite. Some high-intensity peaks consistent with calcite have been detected in LCW-20 point 1 and in LCW-80 point 1. This can be explained by the interference of limestone in the specimen acting as aggregate. It is also observed that smaller peaks are detected consistent with calcite at other points due to carbonation during the experiment.

The interface between the leaching and non-leaching regions is roughly circular because the deterioration effect is equivalent in different directions. The slight fluctuation of the interface was mainly due to the inhomogeneity of hardened cement paste. It can also be observed in Fig.6 that the aggregate is near or even exposed to the dissolution front in some areas. The dissolution front penetrates slightly into the specimen's

interior, implying that the more porous structure of ITZ facilitates deterioration. This phenomenon will be explained in succeeding discussions.



(a) LCW-20 (b) LCW-80

Fig.8 XRD profiles

4.2 Extraction of pore structure

Due to effect of ITZ and leaching, pore structure changes along the direction away from the aggregate surface. Characterizing transport properties at different distance from aggregate is an effective way to study ITZ and leaching deterioration. In order to perform this analysis, it is necessary to extract the pore structure at different distances from the aggregate surface. Fig.9 shows the general process of extracting the pore structure.

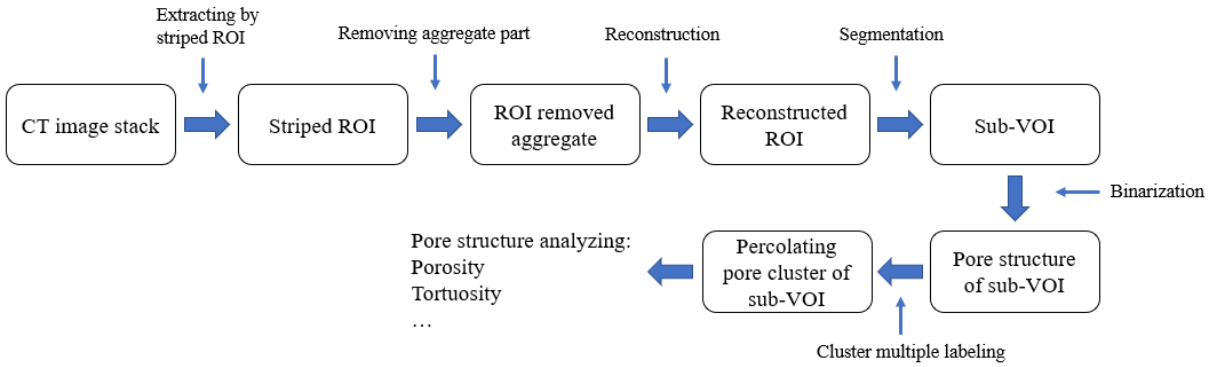
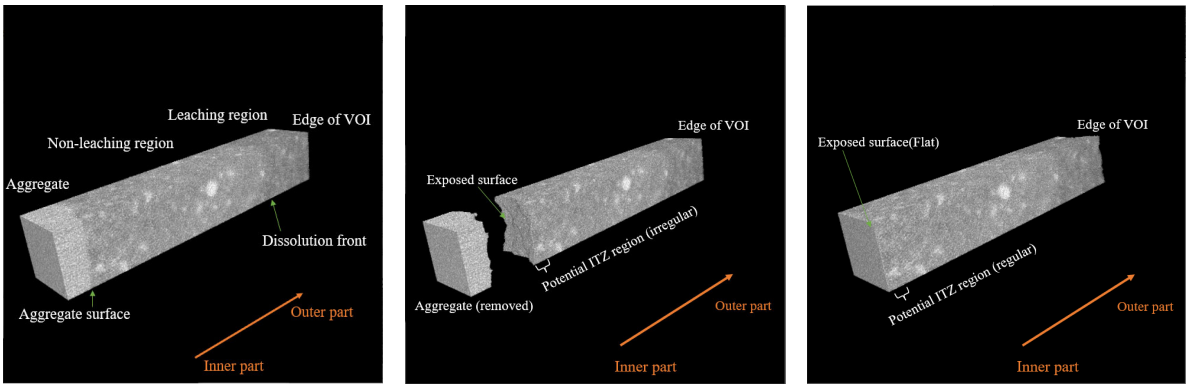


Fig.9 Schematic of extracting the pore structure

In Fig.6, there are three labeled striped ROIs (A, B, and C) in each CT image, and corresponding VOIs will be extracted for further processing. The width of all ROIs is 100 pixels, which makes the size of the cross-section 100×100 pixels. A 3-D view of one of the extracted VOIs is presented in Fig.10(a). In this figure, the surface of aggregate and interface of leaching and non-leaching regions, i.e., the dissolution front, can be clearly seen based on the difference in the grayscale value.



(a)3-D view of extracted VOI (b)Remaining paste part (c) Reconstructed images

Fig.10 Reconstruction of striped ROI (LCW-80, B)

The aggregate component in striped ROI can be easily obtained and isolated based on the difference between the grayscale values of the aggregate and the remaining section. The aggregate part was removed through Boolean operation, which involves subtracting the aggregate part from Fig.10(a). The remaining paste portion is shown in Fig.10(b), where the surface of the bulk hardened cement pastes in contact with the aggregate (also ITZ region adjacent to aggregate) was exposed. Applying reconstruction as mentioned in section 2.2, reconstructed images stack of striped ROI was obtained, and its 3-D view is shown in Fig.10(c).

Through reconstruction, the exposed surface of bulk hardened cement paste was turned into a regular shape. By slicing the striped ROI with a specific thickness along the strip direction, three-dimensional information of cement paste at different distances from the aggregate has been obtained. In this study, these slices with thickness were called sub-VOI. The segmentation of sub-VOI is shown in Fig.11. The size of each sub-VOI is 30×100×100 voxels. The sub-VOI closest to the aggregate surface was set as No.1, and subsequent sub-VOIs were numbered accordingly. The sub-VOI closest to the aggregate, i.e., No.1, contains the 3D information of ITZ in theory, while the rest of the sub-VOI are located in non-leaching and leaching regions, respectively. The locations are based on the positional relationship with the dissolution front. Because of the uncertainty of the ITZ thickness, it is difficult to determine if the No.1 sub-VOI completely covers pure ITZ. However, it can be confirmed that the pore structure of the No.1 sub-VOI is affected by ITZ, to the very least. It should also be noted that the opposite surface of the striped ROI becomes irregular after reconstruction, making it difficult for sub-VOI segmentation to cover the whole striped ROI. Thus, a small portion near the edge cannot be analyzed. This was a compromise that had to be made to analyze the ITZ region. The 3-D pore structure of each sub-VOI was obtained by thresholding the stack of the sub-VOI based on the gray level histogram, which is discussed detailly in previous research[11]. As an example, in the pore structure of No.4 sub-VOI shown in Fig.11, the white voxels (gray level=255) are referred to as the pore, while the black voxels (gray level=0) inside the region of the sub-VOI are referred to as solid. By defining the porosity as the ratio of the number of white voxels to the number of voxels inside the sub-VOI region, each sub-VOI's porosity can be obtained simultaneously.

The pore structure obtained from binarization contains both the connected and isolated pores. Using cluster multiple labeling, the largest connected pore was retained, as illustrated in Fig.11. The connectivity of each sub-VOI can be obtained at the same time by defining the connectivity as the ratio of the numbers of white voxels after cluster multiple labeling to the number of white voxels before cluster multiple labeling.

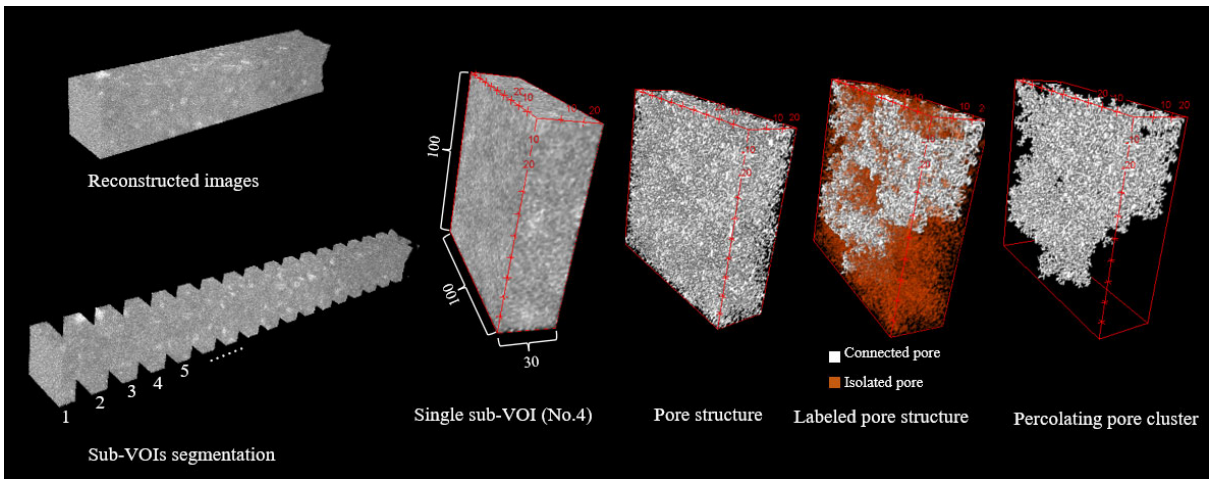


Fig.11 Demonstration of extracting pore structure from sub-VOI

4.3 Tortuosity and diffusion coefficient

As shown in section 3, the computed diffusion tortuosity (τ_D) can be computed using Eq. (1) by applying the random walk simulation to percolating pore cluster of each sub-VOI. This can be further transformed into a diffusion coefficient. To determine the tortuosity, a larger number (N_w) of walkers need to walk freely and randomly in the sub-VOI, and the average of their travel distance over t_∞ must be obtained. Theoretically, both N_w and t_∞ must be sufficiently large, so that the results are statistically meaningful. Hongyan Ma [36] suggested that N_w can be obtained by performing a trial simulation under different number of walkers and by investigating the corresponding convergence of MSD. In this study, $N_w = 10000$ is used. As for t_∞, if t_∞ can ensure that the average traveling distance is comparable to the size of sub-VOI, it can be considered as "sufficiently large", as shown in Eq. (4). In this equation, ρ_e is effective porosity, $F_{esimated}$ is electrical formation factor ($F = D_f/D_e$) estimated before actual conducting random walk simulation, and $L_{sub=VOI}$ is side length of sub-VOI. The size of sub-VOI in this study is 30× 100×100, and according to the conservation principle, $L_{sub-VOI}$ takes 100. $\rho_e F_{esimated}$ can be determined through trial simulation. Because of the different pore structures of the leaching and non-leaching regions, t_∞ was taken from 80000 to 350000, depending on the location of sub-VOIs.

$$t_\infty \approx \rho_e F_{esimated} L_{sub-VOI}^2 \tag{4}$$

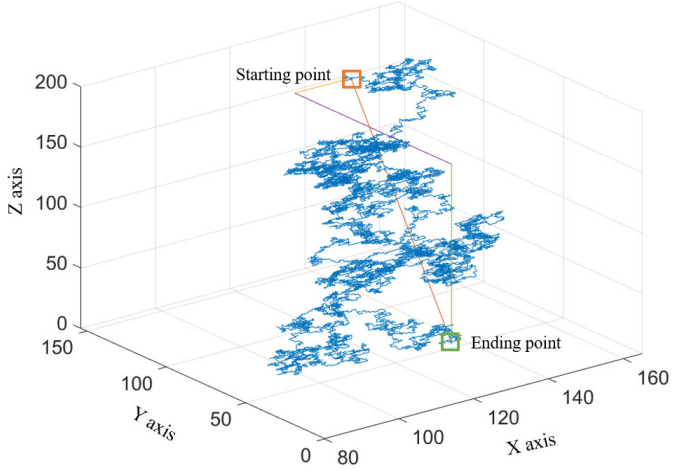


Fig.12 Trajectory of a walker in an extended sub-VOI (200000 steps)

As the starting point and the traveling direction of a walker were randomly selected, it is inevitable for

a walker to walk out of the sub-VOI. By periodical mirror replication, sub-VOI can be extended to the required size. Fig.12 shows the trajectory of a walker in an extended sub-VOI.

The result of the random walk simulation for a given sub-VOI with the determined tortuosity is shown in Fig.13. At the beginning of random walk, trajectory is not yet limited by obstacles, thus MSD-t curve shows unrestricted behavior. As time elapses, walkers migrate further than pore size, and MSD-t curve shows restricted behavior. In the long-time limit, the random walkers fully experience the pore structure and slope of MSD reaches a constant value.[31] Tortuosity can be calculated by Eq.2. The effective diffusion coefficient was calculated by Eq. (3), and the result of each sub-VOI is shown in Fig.14.

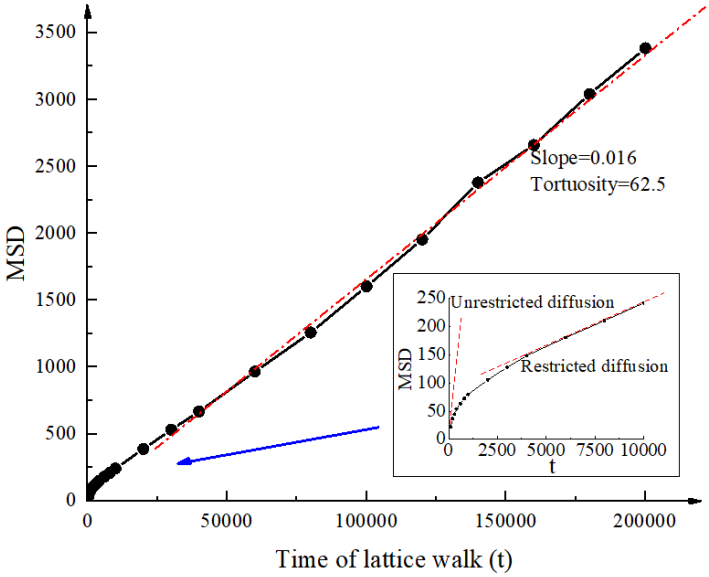
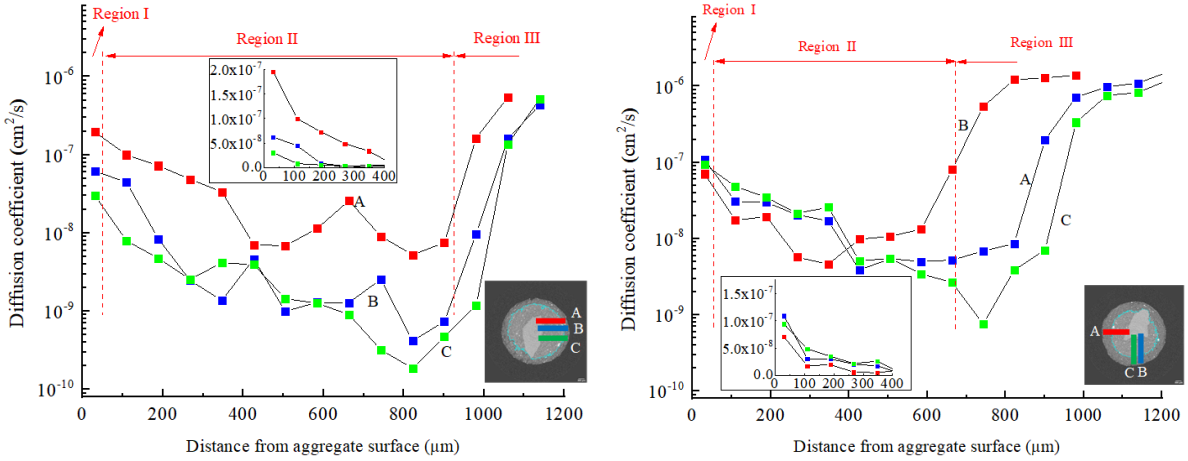


Fig.13 Output of MSD-time relationship in an extended sub-VOI



(a) LCW-20 (b) LCW-80

Fig.14 Computed diffusion coefficient of Ca in each specimen

By analyzing each striped ROI individually for both LCW-20 and LCW-80, the striped ROI can be roughly divided into three regions along the direction away from the aggregate surface, depending on the apparent difference in the computed diffusion coefficient. The segmentation of the three regions is shown in Fig.14 and is labeled as Region I, Region II, and Region III. Region I begins from aggregate surface and ends when the computed diffusion coefficient of a subsequent sub-VOI is less than half of the average diffusion coefficient of all previous sub-VOIs. Segmentation of Region II and III bases difference of computed diffusion coefficient. The computed diffusion coefficient of Region III is much larger than that of Region II, and the boundary between Region II and III highly coincides with the interface between the

leaching region and non-leaching region, i.e., dissolution front in each striped ROI. It should also be noted that when placing the three-striped ROI into one plot for analysis, the boundary between Region I and II coincide well with each other, while the boundary between Region II and III does not. This phenomenon will inevitably appear when the distance from the aggregate surface is used as the coordinate axis because Region I roughly reflects the computed diffusion coefficient near the aggregate surface, while Region II reflects the non-leaching region. Supplementary figures that focus on near aggregate surface in Fig.14 (a) and (b) show rather distinct drop of the diffusion coefficients between Region I and Region II, respectively. Thus, in this study, Region I, Region II, and Region III correspond to the ITZ, non-leaching, and leaching regions, respectively. In addition, specimens subjected to different leaching temperature shows the following difference in Fig.14: diffusion coefficient of region III is higher in LCW-80, and the scope of region III is also larger in LCW-80.

Table 1 shows the computed result of the Ca diffusion coefficient for each region and each specimen. The average of the diffusion coefficients was computed using the corresponding sub-VOIs in each region given in Fig.14. In the previous research, the estimated thickness of ITZ ranged from 9μm to 300μm [39][40][41]. In this study, the thickness of each sub-VOI is 30 pixels, resulting in an actual thickness of 73.8μm for one sub-VOI. The diffusion coefficient in the ITZ determined in this study is within the range of the previously reported values in the literatures.

Table 1 Computed result of Ca diffusion coefficient (cm^2/s)

Specimens	ITZ	Non-leaching region	Leaching region
LCW-20	9.63×10^{-8}	1.17×10^{-8}	4.99×10^{-7}
LCW-80	9.15×10^{-8}	1.12×10^{-8}	1.15×10^{-6}

ITZ without deterioration was framed when selecting ROI in section 4.1, and the computed result in the selected ITZ from LCW-20 and LCW-80 were found to be similar. Furthermore, the diffusion coefficients in non-leaching regions of LCW-20 and LCW-80 are similar. As a result, it can be said that the influence of temperature on Ca diffusion coefficient is significant in leaching region but not large in intact region of the specimen. Summarizing the results, the diffusion coefficient of Ca in non-deteriorated ITZ increases by a factor of 10 when compared to the non-leaching region. The diffusion coefficient of Ca in the leaching region is approximately 50 times that of the non-leaching region in the LCW-20 specimen and approximately 100 times in the LCW-80 specimen. Higher diffusion coefficients of Ca in the leaching region for LCW-80 correlate to a larger accumulated amount of Ca ions, as shown in Fig.4. This is attributed to the promoted dissolution of hydration products due to higher temperature.

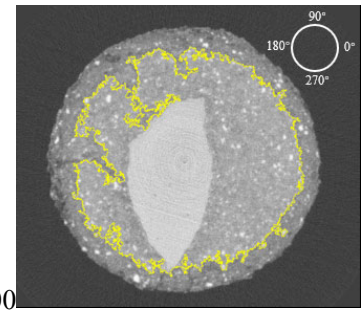
4.4 Effect of ITZ on the leaching process

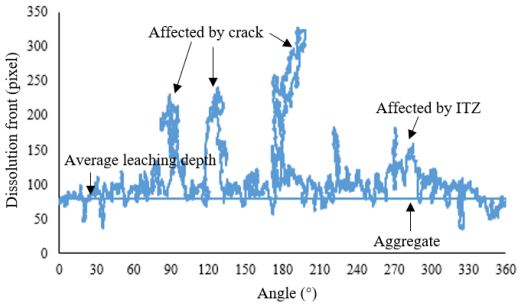
The rate of leaching, which is embodied as the depth of dissolution front, is highly correlated with the permeability of cementitious materials. Thus, theoretically, the existence of more porous ITZ compared to bulk hardened cement paste would cause the leaching region to intrude into the specimen along the aggregate surface. Fig.15 and Fig.16 illustrate different slices of the extracted stack from LCW-20 and LCW-80, in which the dissolution front is marked by the yellow line, based on the grayscale value difference between the leaching region and non-leaching region. Slices with aggregate exposed at or near the dissolution front were selected here to investigate the effect of ITZ on the leaching process. Counterclockwise scanning the entire slice in polar coordinates beginning from due east direction (three o'clock, in another way) and measuring the depth of dissolution front simultaneously, the depth-direction relationship can be obtained and shown on the right.

For every selected slice, the average depth of the dissolution front was shown on the corresponding

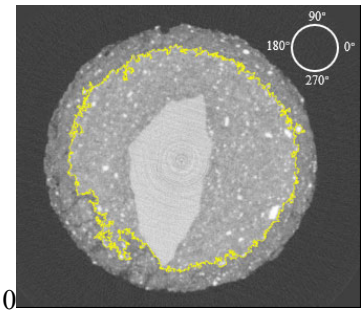
depth-direction curve. The average dissolution front depth of LCW-80 was higher than that of LCW-20, which was also verified on CT images. For both LCW-20 and LCW-80, the depth of the dissolution front fluctuates slightly within the average depth in the direction governed by the normal leaching process (i.e., direction not affected by cracks or aggregate). There are peaks in some directions which are not under the effect of the aggregate, such as in 90°, 120° and 180° of LCW-20 slice 700 and 30° of LCW-20 slice 790. CT images show small cracks in this direction. These cracks could accelerate the leaching process, which may lead to a deeper dissolution front. Crack appearing inside the specimen may be caused by shrinkage. Regardless of the interference of the crack, peaks are present in all slices of LCW-20 in the direction of 270°. This is mainly attributable to the aggregate close to the dissolution front and the ITZ with a more porous structure, which makes it easier to be degraded in this direction. In LCW-80, all slices showed a "U" shape trend in the direction around 60°. This "U" shape is due to the aggregate exposed to the dissolution front, while the peaks on both sides are due to the existence of ITZ, making the dissolution front go deeper inside the specimen along the aggregate surface. It is also observed that the "U" shape for LCW-80 slice 640 is not completely symmetrical, containing only one side peak. Because of the strike direction of the aggregate, the thickness of ITZ on both sides was not generally the same, which resulted in the different progression of the dissolution on both sides of the aggregate.

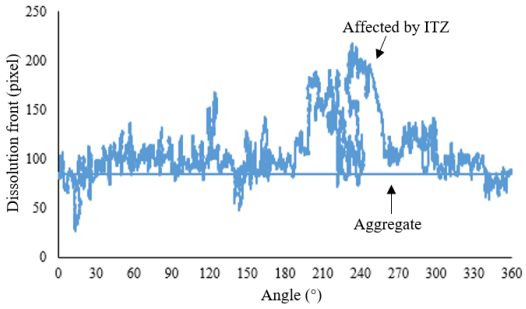
Slice=700



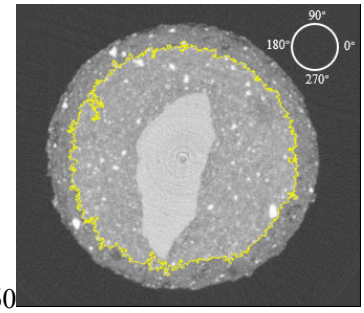


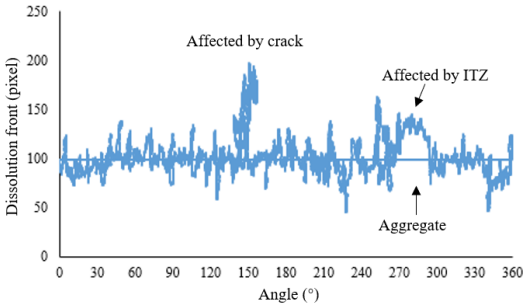
Slice=730





Slice=760





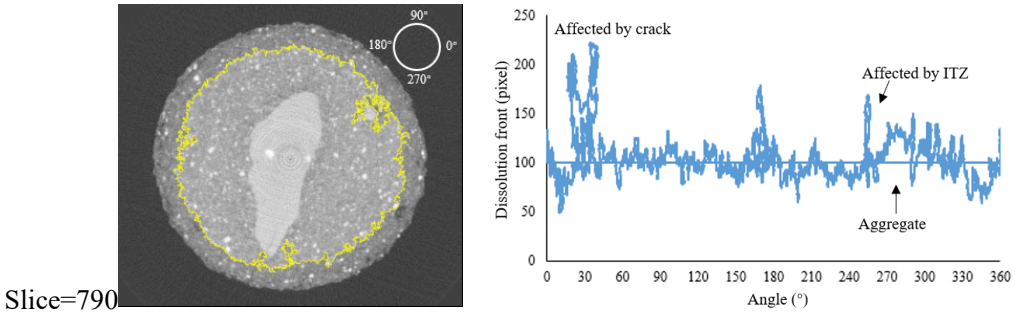


Fig.15 Dissolution front of different slice of LCW-20

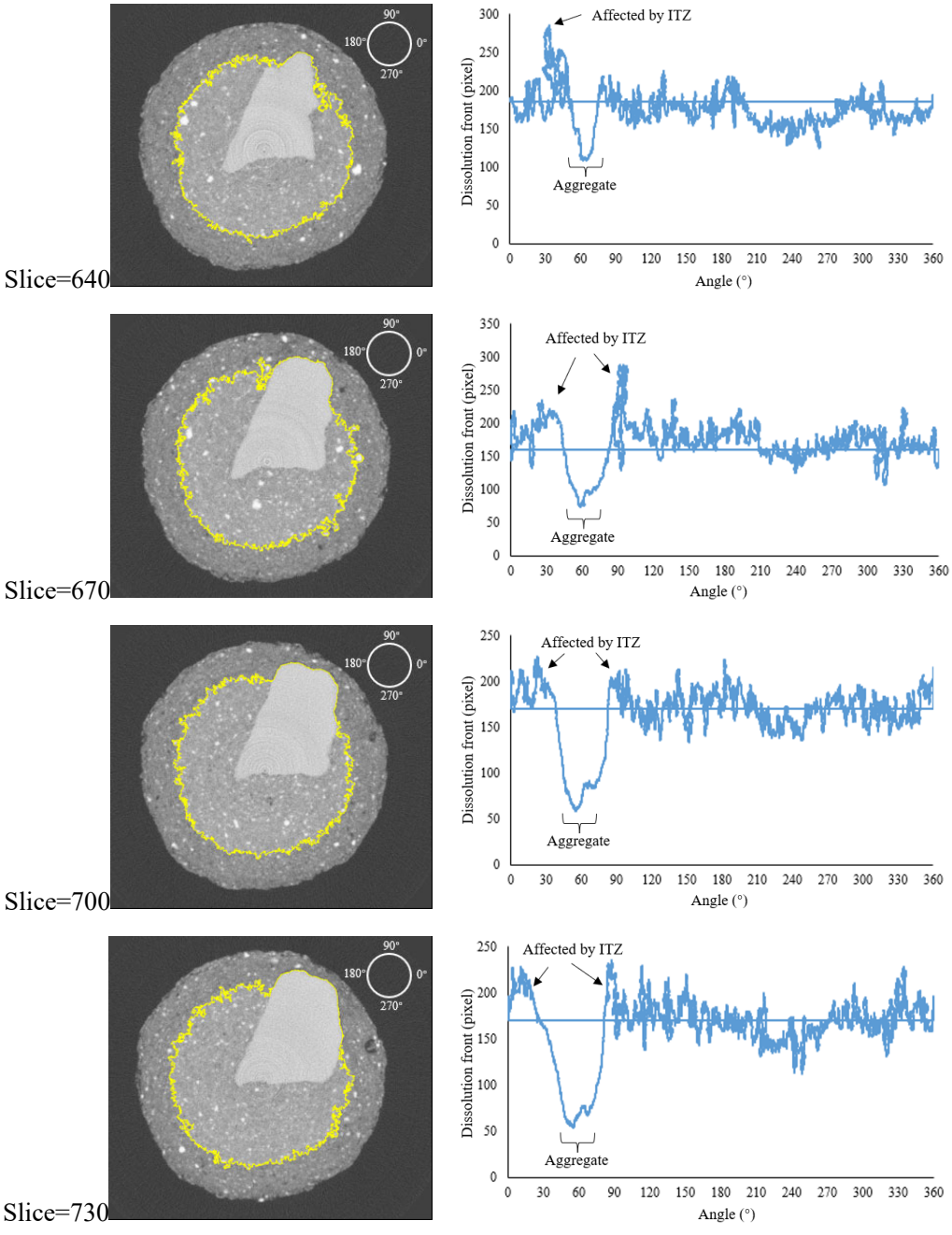


Fig.16 Dissolution front of different slices of LCW-80

5. Conclusion

The following conclusions are drawn based on the results of this research:

(1) The integrated CT-XRD method has been successfully used to evaluate the leaching of calcium ions. This enables experimental analysis on the micrometer order using a minute specimen in a shorter period of 33 days.

(2) A leaching experiment of cement paste containing a single aggregate was carried out. The leaching and non-leaching regions were defined separately based on the difference in the CT values inside the specimen using the X-ray CT method. The leaching region with smaller linear attenuation coefficients is wider with increased temperature from 20℃ to 80℃. This is consistent with the principle that higher temperature results in a larger amount of leaching calcium ions. In addition, from the results of XRD analysis, it is inferred that the peak of portlandite is more prominent in the non-leached region than in the leached region. Hence, portlandite is leached from the leaching region.

(3) Using random walk simulation, it has been determined that the diffusion coefficient within the leaching region is about 50 times larger than in the non-leaching region. On the other hand, the diffusion coefficient within the ITZ is about ten times greater than in the non-leaching region. When the temperature is increased to 80℃, the diffusion coefficient within the leaching region is about 100 times more than in the non-leaching region.

(4) The dissolution front appears deeper inside the specimen in the direction where the aggregate is close to or exposed to the dissolution front. This is because the ITZ is more porous and has a better-connected pore structure than the non-deteriorated bulk cement paste, accelerating the leaching process.

Acknowledgment

Part of this research was funded by the Japan Society for Promotion of the Science (JSPS KAKENHI Grant Number 21H01402) and the Nuclear Safety Research Association. The synchrotron radiation experiments were performed at the BL28B2 in SPring-8 with the approval of the Japan Synchrotron Radiation Research Institute (JASRI) (Proposal No. 2021B1025, 2022A1662).

References

[1] Carde Christophe, and Raoul François. “Effect of the leaching of calcium hydroxide from cement paste on mechanical and physical properties.” Cement and Concrete Research 27.4 (1997): 539-550.

[2] Hiroshi Saito, and Akira Deguchi. “Leaching tests on different mortars using accelerated electrochemical method.” Cement and Concrete Research 30.11 (2000): 1815-1825.

[3] Kazuko Haga, Shunkichi Sutou, Michihiko Hironaga, Satoru Tanaka, and Shinya Nagasaki. “Effects of porosity on leaching of Ca from hardened ordinary Portland cement paste.” Cement and concrete research 35.9 (2005): 1764-1775.

[4] Jacques Marchand, Dale P. Bentz, Eric Samson, and Yannick Maltais. “Influence of calcium hydroxide dissolution on the transport properties of hydrated cement systems.” Reactions of calcium hydroxide in concrete. Westerville, OH: American Ceramic Society (2001): 113-129.

[5] Hayato Takahashi and Takafumi Sugiyama, Investigation of alteration in deteriorated mortar due to water attack using non-destructive integrated CT-XRD method, Proceedings of the 11th fib International Ph.D. Symposium in Civil Engineering, pp. 445-451, 2016

[6] Michael Angelo B. Promentilla, Shermaine M. Cortez, Regina Anne DC. Papel, Bernadette M. Tablada, Takafumi Sugiyama. “Evaluation of microstructure and transport properties of deteriorated cementitious materials from their X-ray computed tomography (CT) images.” Materials 9.5 (2016): 388.

[7] P. Kumar Mehta, and Paulo J.M. Monteiro. Concrete: microstructure, properties, and materials. McGraw-Hill Education, 2014.
[8] Ivan Sandi Darma, Takafumi Sugiyama, and Michael Angelo B. Promentilla. “Application of X-ray CT to study diffusivity in cracked concrete through the observation of tracer transport.” Journal of advanced concrete technology 11.10 (2013): 266-281.
[9] Dale P. Bentz, Daniel A Quenard, H. M. Kunzel, J. Baruchel, F. Peyrin, N. S. Martys, and E. J. Garboczi. “Microstructure and transport properties of porous building materials. II: Three-dimensional X-ray tomographic studies.” Materials and Structures 33.3 (2000): 147-153.
[10] L. Helfen, F. Dehn, P. Mikulík, and T. Baumbach. “Three-dimensional imaging of cement microstructure evolution during hydration.” Advances in Cement Research 17.3 (2005): 103-111.
[11] Michael Angelo B. Promentilla, Takafumi Sugiyama, Takashi Hitomi, and Nobufumi Takeda. “Characterizing the 3D pore structure of hardened cement paste with synchrotron microtomography.” Journal of Advanced Concrete Technology 6.2 (2008): 273-286.
[12] Mingzhong Zhang, and Andrey P. Jivkov. “Micromechanical modelling of deformation and fracture of hydrating cement paste using X-ray computed tomography characterisation.” Composites Part B: Engineering 88 (2016): 64-72.
[13] Hayato Takahashi, and Takafumi Sugiyama. “Application of non-destructive integrated CT-XRD method to investigate alteration of cementitious materials subjected to high temperature and pure water.” Construction and building materials 203 (2019): 579-588.
[14] Mingzhong Zhang, Yongjia He, Guang Ye, David A. Lange, and Klaas van Breugel. “Computational investigation on mass diffusivity in Portland cement paste based on X-ray computed microtomography (μCT) image.” Construction and Building Materials 27.1 (2012): 472-481.
[15] A Cecen, E. A. Wargo, A. C. Hanna, D. M. Turner, S. R. Kalidindi, and E. C Kumbur. “3-D microstructure analysis of fuel cell materials: spatial distributions of tortuosity, void size and diffusivity.” Journal of The Electrochemical Society 159.3 (2012): B299.
[16] Michael Angelo B. Promentilla, Takafumi Sugiyama, Takashi Hitomi, and Nobufumi Takeda. “Quantification of tortuosity in hardened cement pastes using synchrotron-based X-ray computed microtomography.” Cement and Concrete Research 39.6 (2009): 548-557.
[17] Göran Hedenblad. “The use of mercury intrusion porosimetry or helium porosity to predict the moisture transport properties of hardened cement paste.” Advanced Cement Based Materials 6.3-4 (1997): 123-129.
[18] Rachid Cherif, Ameur El Amine Hamami, and Abdelkarim Aït-Mokhtar. “Effects of leaching and chloride migration on the microstructure and pore solution of blended cement pastes during a migration test.” Construction and Building Materials 240 (2020): 117934.
[19] Qinglei Yu, Hongyuan Liu, Tianhong Yang, and Honglei Liu. “3D numerical study on fracture process of concrete with different ITZ properties using X-ray computerized tomography.” International Journal of Solids and Structures 147 (2018): 204-222.
[20] Kai Wu, Huisheng Shi, Linglin Xu, Guang Ye, and Geert De Schutter. “Microstructural characterization of ITZ in blended cement concretes and its relation to transport properties.” Cement and Concrete Research 79 (2016): 243-256.
[21] Juan Lizarazo-Marriaga, Camilo Higuera, and Peter Claisse. “Measuring the effect of the ITZ on the transport related properties of mortar using electrochemical impedance.” Construction and Building Materials 52 (2014): 9-16.
[22] Jianjun Zheng, Hong S. Wong, and Nick R. Buenfeld. “Assessing the influence of ITZ on the steady-state chloride diffusivity of concrete using a numerical model.” Cement and Concrete Research 39.9 (2009):

805-813.
[23] Christophe Carde, Raoul François, and Jean-Michel Torrenti. “Leaching of both calcium hydroxide and CSH from cement paste: Modeling the mechanical behavior.” Cement and concrete research 26.8 (1996): 1257-1268.
[24] Emmanuel Rozière, Ahmed Loukili, Rana EI-Hachem, and Frédéric Grondin. “Durability of concrete exposed to leaching and external sulphate attacks.” Cement and Concrete Research 39.12 (2009): 1188-1198.
[25] Stanley R. Deans. The Radon transform and some of its applications. Courier Corporation, 2007.
[26] Kentaro Uesugi, Yoshio Suzuki, Naoto Yagi, Akira Tsuchiyama, and Tsukasa Nakano. “Development of high spatial resolution X-ray CT system at BL47XU in SPring-8.” Nuclear Instruments and Methods in Physics Research Section A: Accelerators, Spectrometers, Detectors and Associated Equipment 467 (2001): 853-856.
[27] Dale P. Bentz, Symoane Mizell, Steve Satterfield, Judith Devaney, William George, Peter Ketcham, James Graham, and James Porterfield. “The visible cement data set.” Journal of Research of the National Institute of Standards and Technology 107.2 (2002): 137.
[28] S. Lu, E. N. Landis, and D. T. Keane. “X-ray microtomographic studies of pore structure and permeability in Portland cement concrete.” Materials and structures 39.6 (2006): 611-620.
[29] M Koster, J. Hannawald, and W. Brameshuber. “Simulation of water permeability and water vapor diffusion through hardened cement paste.” Computational mechanics 37.2 (2006): 163-172.
[30] S Ikeda, T. Nakano, and Y. Nakashima. “Three-dimensional study on the interconnection and shape of crystals in a graphic granite by X-ray CT and image analysis.” Mineralogical Magazine 64.5 (2000): 945-959.
[31] Yoshito Nakashima, and Susumu Kamiya. “Mathematica programs for the analysis of three-dimensional pore connectivity and anisotropic tortuosity of porous rocks using X-ray computed tomography image data.” Journal of Nuclear Science and Technology 44.9 (2007): 1233-1247.
[32] Takafumi Sugiyama, and Michael Angelo B. Promentilla. “Advancing Concrete Durability Research through X-ray Computed Tomography.” Journal of Advanced Concrete Technology 19.6 (2021): 730-755.
[33] Takafumi Sugiyama, Michael Angelo B. Promentilla, and Nobufumi Takeda. “Application of synchrotron microtomography for pore structure characterization of deteriorated cementitious materials due to leaching.” Cement and Concrete Research 40.8 (2010): 1265-1270.
[34] Pabitra N. Sen. “Time-dependent diffusion coefficient as a probe of geometry.” Concepts in Magnetic Resonance Part A: An Educational Journal 23.1 (2004): 1-21.
[35] Lawrence L Latour, Robert L Kleinberg, Partha P Mitra, and Christopher H Sotak. “Pore-size distributions and tortuosity in heterogeneous porous media.” Journal of Magnetic Resonance, Series A 112.1 (1995): 83-91.
[36] Hongyan Ma, Dongshuai Hou, and Zongjin Li. “Two-scale modeling of transport properties of cement paste: Formation factor, electrical conductivity and chloride diffusivity.” Computational Materials Science 110 (2015): 270-280.
[37] Niels Iversen, and Bo Barker Jørgensen. “Diffusion coefficients of sulfate and methane in marine sediments: Influence of porosity.” Geochimica et Cosmochimica Acta 57.3 (1993): 571-578.
[38] Ana C.F. Ribeiro, Marisa C.F. Barros, Ana S.N. Teles, Artur J.M. Valente, Victor M.M. Lobo, Abílio J.F.N. Sobral, M.A. Esteso. “Diffusion coefficients and electrical conductivities for calcium chloride aqueous solutions at 298.15 K and 310.15 K.” Electrochimica Acta 54.2 (2008): 192-196.
[39] Jean Pierre Ollivier, Jean Claude Maso, and B. Bourdette. “Interfacial transition zone in concrete.” Advanced cement based materials 2.1 (1995): 30-38.

[40] Mirshad Maleki, Iraj Rasoolan, Amin Khajehdezfuly, and Andrey P. Jivkov. “On the effect of ITZ thickness in meso-scale models of concrete.” Construction and Building Materials 258 (2020): 119639.
[41] Hiroaki Hasebe, Akio Chimoto, and Takafumi Sugiyama “Evaluation of Interfacial Transition Zone in Concrete by Synchrotron Radiation Microtomography”, Proceedings of the 6th International Conference on Construction Materials (ConMat’20), pp.755-765, sept. 2020